

# Path-optimized nonadiabatic geometric quantum computation on superconducting qubits

Cheng-Yun Ding,<sup>1</sup> Li-Na Ji,<sup>1</sup> Tao Chen,<sup>1</sup> and Zheng-Yuan Xue<sup>1,2,3,\*</sup>

<sup>1</sup>*Guangdong Provincial Key Laboratory of Quantum Engineering and Quantum Materials, and School of Physics and Telecommunication Engineering, South China Normal University, Guangzhou 510006, China*

<sup>2</sup>*Guangdong-Hong Kong Joint Laboratory of Quantum Matter, Frontier Research Institute for Physics, South China Normal University, Guangzhou 510006, China*

<sup>3</sup>*Guangdong Provincial Key Laboratory of Quantum Science and Engineering, Southern University of Science and Technology, Shenzhen, Guangdong 518055, China*

(Dated: March 20, 2022)

Quantum computation based on nonadiabatic geometric phases has attracted a broad range of interests, due to its fast manipulation and inherent noise resistance. However, to obtain universal geometric quantum gates, the required evolution paths are usually limited to some special ones, and the evolution times of which are still longer than dynamical quantum gates, resulting in weakening of robustness and more infidelity of the implemented geometric gates. Here, we propose a path-optimized scheme for geometric quantum computation on superconducting transmon qubits, where high-fidelity and robust universal nonadiabatic geometric gates can be implemented, based on conventional experimental setups. Specifically, we find that, by selecting appropriate evolution paths, the constructed geometric gates can be superior to their corresponding dynamical ones under different local errors. Through our numerical simulations, we obtain the fidelities for single-qubit geometric Phase,  $\pi/8$  and Hadamard gates as 99.93%, 99.95% and 99.95%, respectively. Remarkably, the fidelity for two-qubit control-phase gate can be as high as 99.87%. Therefore, our scheme provides a new perspective for geometric quantum computation, making it more promising in the application of large-scale fault-tolerant quantum computation.

---

\* zyxue83@163.com

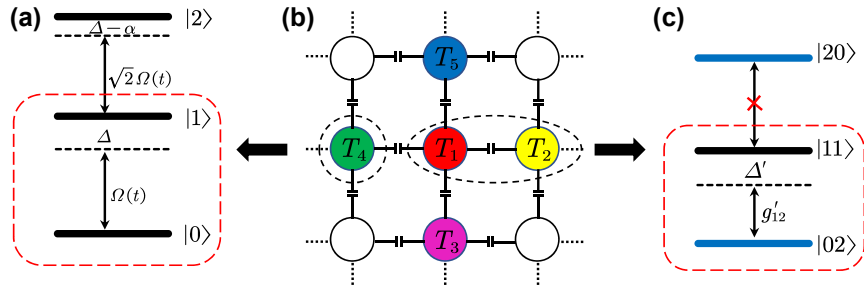


FIG. 1. Illustration of our implementation. (a) The energy spectrum diagram for a driven transmon qubit  $T_4$  with the detuning  $\Delta$  and the weak anharmonicity  $\alpha$ . (b) Schematic diagram of a 2D square transmon lattice linked by coupling capacitively, and the transmon qubits  $T_1 \sim T_5$  with different colors have different frequencies. (c) The level structure of second excitation subspace for two parametrically tunable coupled transmons  $T_1$  and  $T_2$  with a small detuning  $\Delta'$  between energy levels  $|11\rangle$  and  $|02\rangle$ .

## I. INTRODUCTION

It is well-known that the physical realization of quantum computers needs a set of universal quantum logic gates, which includes a set of arbitrary single-qubit gates and a nontrivial two-qubit gate [1, 2]. However, the coherence of quantum system can be easily ruined by its surrounding environment, invalidating the computation process. Therefore, the fidelity of quantum gates must be high enough so that quantum error correction can be applied to achieve large-scale quantum computation. Moreover, beyond the error-correction threshold, the higher gate-fidelity can result in fewer physical qubit resources encoding an error-free logical qubit. In addition, local random and control errors can also be occurred during the manipulation of the quantum system. Thus, it is also vital to find a robust way of quantum control that is insensitive to these local errors.

One of the promising ways to obtain strong robust quantum gates is suggested to use geometric phase, which was first discovered by Berry [3] based on adiabatic process. The geometric phase has global characteristics which only depends on the area of evolution path instead of the evolution details. Thus, quantum gates based on the geometric phase have the intrinsic merit of being robust against local systematic errors, and thereby geometric quantum computation (GQC) [4] was received extensively studied with experimentally demonstrations [5–7]. However, the required adiabatic evolution condition there makes operational time of geometric gates to be much longer than that of conventional quantum gates using dynamical evolution, and thus the gate-fidelity is very low in typical quantum systems. In 1987, to remove the constraint of the adiabatic condition, Aharonov and Anandan [8] generalize the adiabatic Berry phase to nonadiabatic case. Then, nonadiabatic GQC schemes were proposed [9–11] and verified experimentally [12–14], which can greatly speed up the geometric gates. Besides, the Berry phase has also been generalized to non-Abelian case [15], which also found many applications in quantum computation [16–20]. These advances thus make GQC to be a promising way towards robust quantum manipulation [21–25].

As we all know, the total phase during quantum evolution consists of both the dynamical and geometric parts. To get a pure geometric phase, the usual method is to eliminate the accompanied dynamical phase, which can be achieved via several special evolution loops [26–28], besides the original time-consuming multi-loop evolution strategies. Therefore, the schemes of GQC based on single-loop evolution have been proposed [29–37], which further decreases the needed time for geometric gates. Notably, the elimination of dynamical phase has also been investigate in the case of quantum computation with non-cyclic geometric phases [38–43].

Here, we demonstrate that a given geometric gate can be obtained from various evolution loops that have the different gate robustness. Thus, we take a novel strategy of constructing geometric gates by proposing a path-optimized scheme to realize nonadiabatic GQC and present its implementation on superconducting transmon qubits [44, 45]. Besides, we take a set of universal single-qubit geometric gates, i.e., the geometric  $\pi/4$ ,  $\pi/8$   $Z$ -rotation and Hadamard gates, denoted as S, T and H, respectively, as typical examples to test the gate fidelity and robustness. The numerical simulations show that our geometric gates have stronger robustness than the corresponding dynamical gates in certain parametric ranges. Similarly, this path-optimized method can also be readily extended to the case of nontrivial two-qubit geometric gates. Therefore, our scheme provides a new perspective for geometric quantum gates, making them being more promising in future large-scale fault-tolerant quantum computation.

## II. GEOMETRIC GATES WITH PATH OPTIMIZATION

In this section, we first present the construction of arbitrary single-qubit nonadiabatic geometric gates on a superconducting transmon qubit with conventional control technology, showing that from our construction, a given geometric gate can be achieved by different evolution paths. Second, we take geometric S, T and H gates as typical examples to test the gate robustness

under different evolution paths, which demonstrates that the robustness is different under different paths. Thus, we compare the robustness based on several selected paths with the corresponding dynamical gates, and indicate that our scheme has an advantage range where the robustness of geometric gates is superior to dynamical one. Finally, based on the optimal evolution path, we evaluate these gates performance within actual experimental parameters.

### A. The nonadiabatic geometric phases

Superconducting quantum circuit system is one of the most promising physical platforms to realize universal quantum computation, due to its flexible controllability and easy scalability. Thanks to the long coherence time, superconducting transmon qubits are usually used to encode quantum information. The energy spectrum for a transmon qubit is shown in figure 1(a), which has a weak anharmonicity labelled as  $\alpha$ . For the general requirement of scalable quantum computation, we consider a 2D square lattice of transmon qubits, where all the adjacent transmons are capacitively coupled, as shown in figure 1(b). The Hamiltonian of a transmon qubit interacting with an external driving microwave field can be described as

$$\mathcal{H}(t) = \omega_0|1\rangle\langle 1| + (2\omega_0 - \alpha)|2\rangle\langle 2| + \frac{1}{2}\left\{\Omega(t)e^{i[\omega(t)\cdot t - \phi(t)]}(|0\rangle\langle 1| + \sqrt{2}|1\rangle\langle 2|) + \text{H.c}\right\}, \quad (1)$$

where  $\omega_0$  is transition frequency of the transmon qubit with the energy of ground state setting to be zero,  $\Omega(t)$ ,  $\omega(t)$  and  $\phi(t)$  are driving strength, frequency and phase of microwave field, respectively. Note that we here use  $\{|0\rangle, |1\rangle\}$  as our computational subspace, and consider the higher energy level  $|2\rangle$  as the main leakage source, due to the weak anharmonicity of transmon qubit. Applying a representation transformation of  $U = U_2 \times U_1$  to the Hamiltonian in equation (1) with  $U_1 = \exp\{-i\omega_0(|1\rangle\langle 1| + 2|2\rangle\langle 2|)t\}$ ,  $U_2 = \exp\{i\Delta(t)(|1\rangle\langle 1| - |0\rangle\langle 0| + 3|2\rangle\langle 2|)t/2\}$ , the transformed Hamiltonian  $\mathcal{H}'(t)$  will be

$$\mathcal{H}'(t) = \frac{1}{2}\{\Delta(t)(|1\rangle\langle 1| - |0\rangle\langle 0| + 3|2\rangle\langle 2|) - 2\alpha|2\rangle\langle 2|\} + \frac{1}{2}\left\{\Omega(t)e^{-i\phi(t)}(|0\rangle\langle 1| + \sqrt{2}|1\rangle\langle 2|) + \text{H.c}\right\}, \quad (2)$$

where the detuning is defined as  $\Delta(t) = \omega_0 - \omega(t)$ .

Next, we consider the ideal case, i.e., projecting the Hamiltonian  $\mathcal{H}'(t)$  within the qubit subspace, to show the construction of arbitrary single-qubit nonadiabatic geometric gates with path optimization. Then, the Hamiltonian  $\mathcal{H}'(t)$  can be reduced to

$$\mathcal{H}_1(t) = -\frac{1}{2}\{\Delta(t)\sigma_z - \Omega(t)[\cos\phi(t)\sigma_x + \sin\phi(t)\sigma_y]\}, \quad (3)$$

with  $\{\sigma_x, \sigma_y, \sigma_z\}$  being well-known Pauli operators. We further choose a set of dressed-state bases  $\{|\varphi_{\pm}(t)\rangle\}$  as the evolution states which are, respectively,

$$\begin{aligned} |\varphi_+(t)\rangle &= e^{ik_+(t)}[\cos(\chi(t)/2)|0\rangle + \sin(\chi(t)/2)e^{i\xi(t)}|1\rangle], \\ |\varphi_-(t)\rangle &= e^{ik_-(t)}[\sin(\chi(t)/2)e^{-i\xi(t)}|0\rangle - \cos(\chi(t)/2)|1\rangle], \end{aligned} \quad (4)$$

where  $k_{\pm}(t)$  satisfy  $k_{\pm}(0)=0$ , and their evolution trajectories on the Bloch sphere can be determined by the time-dependent polar angle  $\chi(t)$  and azimuth angle  $\xi(t)$ . By solving the Schrödinger equation  $i|\dot{\varphi}_{\pm}(t)\rangle = \mathcal{H}_1(t)|\varphi_{\pm}(t)\rangle$ , we can get the parameters that determine the evolution trajectories as

$$\dot{\chi}(t) = \Omega(t)\sin[\phi(t) - \xi(t)], \quad \dot{\xi}(t) = -\Delta(t) - \Omega(t)\cot\chi(t)\cos[\phi(t) - \xi(t)], \quad (5)$$

as well as

$$k_+(t) = -k_-(t) = -\frac{1}{2}\int_0^t\left\{\dot{\xi}(t')[\cos\chi(t') - 1] - \Delta(t')\right\}/\cos\chi(t')dt'. \quad (6)$$

Assuming that the evolution trajectory is determined, which corresponds to the known polar and azimuth angles, then the relevant parameters  $\{\Omega(t), \phi(t), \Delta(t)\}$  of Hamiltonian  $\mathcal{H}_1(t)$  can be obtained reversely by solving the above restriction relations. Therefore, after a period of cyclic evolution  $\tau$ , the evolution states will be transformed into  $U(\tau)|\varphi_{\pm}(0)\rangle = e^{ik_{\pm}(\tau)}|\varphi_{\pm}(0)\rangle$ , whose corresponding evolution operator is

$$\begin{aligned} U(\tau) &= e^{ik_+(\tau)}|\varphi_+(0)\rangle\langle\varphi_+(0)| + e^{ik_-(\tau)}|\varphi_-(0)\rangle\langle\varphi_-(0)| \\ &= \cos\gamma + i\sin\gamma[\sigma_z\cos\chi_0 + \sin\chi_0(\sigma_x\cos\xi_0 + \sigma_y\sin\xi_0)] = e^{i\gamma\vec{n}\cdot\vec{\sigma}}, \end{aligned} \quad (7)$$

where  $\gamma = k_+(\tau) = -k_-(\tau) = \gamma_d + \gamma_g$  is the accumulated total phase during the evolution process,  $\chi_0 = \chi(0)$  and  $\xi_0 = \xi(0)$  are the initial polar and azimuth angles, respectively. Since  $\vec{n} = (\sin\chi_0\cos\xi_0, \sin\chi_0\sin\xi_0, \cos\chi_0)$  is an arbitrary unit direction

vector and  $\vec{\sigma} = (\sigma_x, \sigma_y, \sigma_z)$  is a vector for Pauli operators,  $U(\tau)$  represents a rotation along the  $\vec{n}$  axis with an angle of  $-2\gamma$ . In addition, as the dynamical phase  $\gamma_d$  can be calculated as

$$\gamma_d = - \int_0^\tau \langle \varphi_+(t) | \mathcal{H}_1(t) | \varphi_+(t) \rangle dt = \frac{1}{2} \int_0^\tau [\dot{\xi}(t) \sin^2 \chi(t) + \Delta(t)] / \cos \chi(t) dt, \quad (8)$$

the remaining geometric phase  $\gamma_g$  will be

$$\gamma_g = \gamma - \gamma_d = -\frac{1}{2} \int_0^\tau \dot{\xi}(t) [1 - \cos \chi(t)] dt. \quad (9)$$

Quantum logic gates constructed by geometric phases have intrinsic fault-tolerance feature, as the geometric phase only depend on the global geometric properties of the path, instead of the specific evolution details. This can be explained by the fact that, in equation (9), the geometric phase is equal to half of the solid angle enclosed by the evolution path. However, the existence of dynamical phase, as shown in equation (8), leads to the appearance of a non-geometric component in the total phase, which will destroy the global noise-resistance feature of the constructed geometric gate, and thus need be eliminated to get a pure geometric phase.

## B. Construction of path-optimized geometric gates

In this subsection, we consider the construction of path-optimized geometric gates, with the above proposed method of inducing geometric phases. In the above construction, the detuning is set to be in a generally time-dependent form, but we now set it as a constant, following the experimentally preference. That is, we set  $\Delta(t) = \Delta$ , and consider the case that the closed evolution paths are formed by the longitude and latitude lines, for simplicity. In this case, the shapes of parameters  $\{\Omega(t), \phi(t), \Delta(t)\}$  can be reduced to the following equations, by solving the equation (5) and equation (8) (by setting  $\gamma_d = 0$ ) as

$$\Omega(t) = \dot{\chi}(t) / \sin [\phi(t) - \xi], \quad (10a)$$

for the longitude line, and

$$\Omega(t) = -[\dot{\xi}(t) + \Delta] \tan \chi / \cos [\phi(t) - \xi(t)], \quad (10b)$$

for the latitude line. Besides, the constrain for other parameters are as

$$\phi(t) = \xi(t) - \arctan \left\{ \dot{\chi}(t) \cot \chi(t) / [\dot{\xi}(t) + \Delta] \right\}, \quad (11)$$

$$\Delta = -\frac{1}{\tau} \int_0^\tau \dot{\xi}(t) \sin^2 \chi(t) dt. \quad (12)$$

In addition, according to equation (9), the geometric phase  $\gamma_g$  is only related to the polar angle  $\chi(t)$  and the azimuth angle  $\xi(t)$  of the evolution path, and thus different choices of parameters  $\{\chi(t), \xi(t)\}$  may induce the same  $\gamma_g$ . Specifically, if the rotation axis  $\vec{n}$  is determined, i.e., the initial value  $(\chi_0, \xi_0)$  of the evolution state is determined, different evolution paths can be chosen for each specific single-qubit geometric gate.

Thus, as shown in figure 2(a), to realize universal single-qubit nonadiabatic geometric gates, the evolution path can be divided into four parts in the Bloch sphere, and the parameters  $\{\Omega(t), \phi(t), \Delta(t)\}$  of microwave fields in each part must meet the following conditions,

$$\mathcal{S}_1 = \int_0^{\tau_1} \Omega(t) dt = \chi_0, \quad \Delta = 0, \quad \phi = \xi_0 - \frac{\pi}{2}, \quad (13a)$$

$$\mathcal{S}_2 = \int_{\tau_1}^{\tau_2} \Omega(t) dt = \Lambda, \quad \Delta = 0, \quad \phi = \xi_1 + \frac{\pi}{2}, \quad (13b)$$

$$\begin{aligned} \mathcal{S}_3 &= \int_{\tau_2}^{\tau_3} \Omega(t) dt = |\lambda \tan \Lambda \cos^2 \Lambda|, \quad \Delta = \frac{\lambda \sin^2 \Lambda}{\tau_3 - \tau_2}, \\ \phi(t) &= \xi(t) + \pi, \quad 0 < \Lambda < \pi/2; \phi(t) = \xi(t), \pi/2 < \Lambda \leq \pi, \end{aligned} \quad (13c)$$

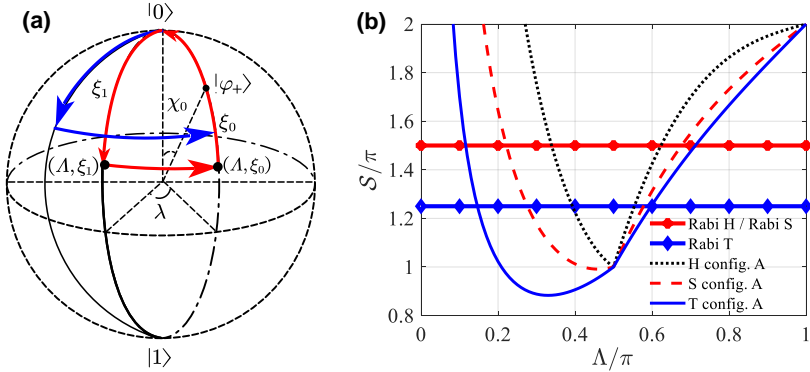


FIG. 2. Illustration of our path-optimized single-qubit geometric gate construction (the configuration A) and the needed pulse area. (a) The closed evolution trajectories for a gate in the Bloch sphere, where different colours denote trajectories with different path parameters  $\Lambda$ . (b) The comparison of pulse areas  $S$  between geometric S, T and H gates with different path parameters and their corresponding dynamical gates.

$$\begin{aligned} S_4 &= \int_{\tau_3}^{\tau} \Omega(t) dt = |\Lambda - \chi_0|, \quad \Delta = 0, \\ \phi &= \xi_0 - \frac{\pi}{2}, \quad \Lambda > \chi_0; \phi = \xi_0 + \frac{\pi}{2}, \quad \Lambda < \chi_0, \end{aligned} \quad (13d)$$

where  $S_i$  denotes the pulse area of the  $i$ th segment,  $\lambda = \xi_1 - \xi_0$ ,  $\Lambda$  equals to value of the polar angle  $\chi(t)$  on the third segment ( $t \in [\tau_2, \tau_3]$ ), which is a constant and  $\Lambda \in (0, \pi/2) \cup (\pi/2, \pi]$ . This choice of  $\xi_1$  leads to an anticlockwise trajectory as shown in figure 2(a), and we term it configuration A. By this setting, at the final time  $\tau$ , the evolution operator will be

$$U_1(\tau) = U_1(\tau, \tau_3)U_1(\tau_3, \tau_2)U_1(\tau_2, \tau_1)U_1(\tau_1, 0) = e^{i\gamma_g \vec{n} \cdot \vec{\sigma}}, \quad (14)$$

which is an arbitrary single-qubit geometric gate and  $\gamma_g = \lambda(1 - \cos \Lambda)/2$  (assuming  $\gamma_g < 0$ ). Since  $\gamma_g$  is only related to  $\Lambda$  and  $\lambda$ , we can choose different evolutionary trajectories to realize the same specific gate under the condition of fixing the evolutionary starting point. For example, shown in figure 2(a), the evolution state  $|\varphi_+(t)\rangle$  can return to the starting point along either path 1 (red line) or path 2 (blue line) to get the same geometric gate. Note that paths 1 and 2 have different  $\Lambda$ , so we term it as the “path parameter”.

Specifically, in order to implement geometric S, T and H gates, we can set

$$\begin{aligned} (\chi_0, \xi_0) &= (0, 0), & \gamma_g &= -\pi/4, \\ (\chi_0, \xi_0) &= (0, 0), & \gamma_g &= -\pi/8, \\ (\chi_0, \xi_0) &= (\pi/4, 0), & \gamma_g &= -\pi/2, \end{aligned} \quad (15)$$

respectively. As it is well-known that the gate sequence of them can construct arbitrary single-qubit geometric gates. Moreover, for a certain  $\gamma_g$ , different choice of parameters  $\{\Lambda, \lambda\}$  corresponds to different evolution paths, with which we can realize the same geometric gate but with different gate-robustness.

In addition, as in figure 2(b), we also consider the needed gate-time of these geometric gates with different path parameters  $\Lambda$ . Here, the gate-time is defined by their corresponding pulse areas  $S = \sum_{i=1}^4 S_i = \int_0^{\tau} \Omega(t) dt$ . Besides, we compare the gate-time in our scheme with the corresponding dynamical one. It can be concluded that geometric S, T and H gates have shorter gate-time than their corresponding dynamical gates within the path parameter ranges of  $\Lambda/\pi \in [0.23, 0.5) \cup (0.5, 0.67]$ ,  $[0.15, 0.5) \cup (0.5, 0.59]$  and  $[0.34, 0.5) \cup (0.5, 0.62]$ , respectively. Significantly, within a fairly wide range of paths, the pulse areas of these gates are less than  $2\pi$  that corresponds to those of the conventional nonadiabatic GQC schemes [31–33], which is also one of the merits of our scheme.

### C. Gate robustness

In the following, we evaluate the gate robustness of the implemented geometric S, T and H gates with path selection. Under the conventional errors against the amplitude deviation of the driving fields and the qubit-frequency drift, i.e.,  $\sigma_x$  and  $\sigma_z$  errors, the Hamiltonian  $\mathcal{H}_1(t)$  will be changed into

$$\mathcal{H}'_1(t) = \frac{1}{2} \begin{pmatrix} -(\Delta + \delta\Omega_0) & \Omega(t)(1 + \epsilon)e^{-i\phi(t)} \\ \Omega(t)(1 + \epsilon)e^{i\phi(t)} & \Delta + \delta\Omega_0 \end{pmatrix}, \quad (16)$$

where  $\epsilon$  and  $\delta$  represent the error fractions for two errors in unit of the time-dependent amplitude  $\Omega(t)$  and its maximum amplitude  $\Omega_0$ , respectively. Besides, we use the definition of gate fidelity, under the two errors [46],

$$F_G^{\epsilon, \delta} = \text{Tr}(U_1^\dagger U_1^{\epsilon, \delta}) / \text{Tr}(U_1^\dagger U_1), \quad (17)$$

to evaluate the gate robustness, where  $U_1^{\epsilon, \delta}$  and  $U_1$  are the evolution operators with and without errors, respectively. In figure 3, we show the gate fidelities of the geometric S, T and H gates as function of path parameter  $\Lambda/\pi \in [0.1, 0.5) \cup (0.5, 1]$  and the two kinds of local errors  $\epsilon, \delta \in [-0.1, 0.1]$ . We can clearly see that the gate robustness is different for different  $\Lambda$ , and we target to find ranges of the path parameter  $\Lambda$ , where the geometric gate-robustness is better than that of the corresponding dynamical one for both errors.

We now compare the robustness between geometric and corresponding dynamical gates (denoted as “Rabi gates”) against two errors, and the construction of the dynamical gates is detailed in appendix A. In figure 4, we plot the boundary paths, i.e., the robustness of both strategies is approximately the same. And, within the boundaries, the robustness of the geometric gates is better than the corresponding dynamical ones. Therefore, we can obtain that the robustness of geometric S and T gates is better than that of the corresponding dynamical gates against both errors within ranges of  $\Lambda/\pi \in [0.3, 0.5) \cup (0.5, 1]$  and  $[0.19, 0.5) \cup (0.5, 1]$ , respectively. For the geometric H gate, its robustness is better than that of the corresponding dynamical gate against  $\sigma_x$  error in the range  $\Lambda/\pi \in [0.3, 0.5) \cup (0.5, 1)$  and that against  $\sigma_z$  error only for the path  $\Lambda/\pi = 1$ , which reduces to the orange-slice-shaped-loop case [31–33]. Remarkably, there is another kind of path configuration, we term it as the “configuration B”, in contrast to the “configuration A” of described above. We find that, for the case of H gate against  $\sigma_z$  error, there is still a parameter range of  $\Lambda/\pi \in [0.65, 0.75]$ , within which geometric H gate has better robustness than the corresponding dynamical gate, and the details are presented in appendix B. So, for quantum systems with different dominant errors, we can utilize the different configuration strategies to construct geometric H gate with strong robustness, extending the robust characteristic for the orange-slice-shape scheme [14] to our shorter path scheme.

#### D. Gate performance on a transmon under decoherence

In practical superconducting system, due to the weak anharmonicity of a transmon qubit, the state population in computational subspace  $\{|0\rangle, |1\rangle\}$  will leak to higher levels, e.g.  $|2\rangle$ , which leads to the decrease of fidelity. Thus, it is necessary to use “derivative removal via adiabatic gate” technique [47, 48] to correct this leakage. Here, we can simulate numerically the gate fidelity by setting appropriate parameters, using the Lindblad master equation [49] of

$$\dot{\rho}_1 = -i[\mathcal{H}(t), \rho_1] + \frac{1}{2} \{ \kappa_z \mathcal{L}(\mathcal{A}_z) + \kappa_- \mathcal{L}(\mathcal{A}_-) \}, \quad (18)$$

where  $\rho_1$  is the density matrix of the quantum system and its quantum dynamics is governed by the Hamiltonian  $\mathcal{H}(t)$ ,  $\mathcal{L}(\mathcal{A}) = 2\mathcal{A}\rho_1\mathcal{A}^\dagger - \mathcal{A}^\dagger\mathcal{A}\rho_1 - \rho_1\mathcal{A}^\dagger\mathcal{A}$  is the Lindblad operator for decay operator  $\mathcal{A}_- = |0\rangle_1\langle 1| + \sqrt{2}|1\rangle_1\langle 2|$  and dephasing operator

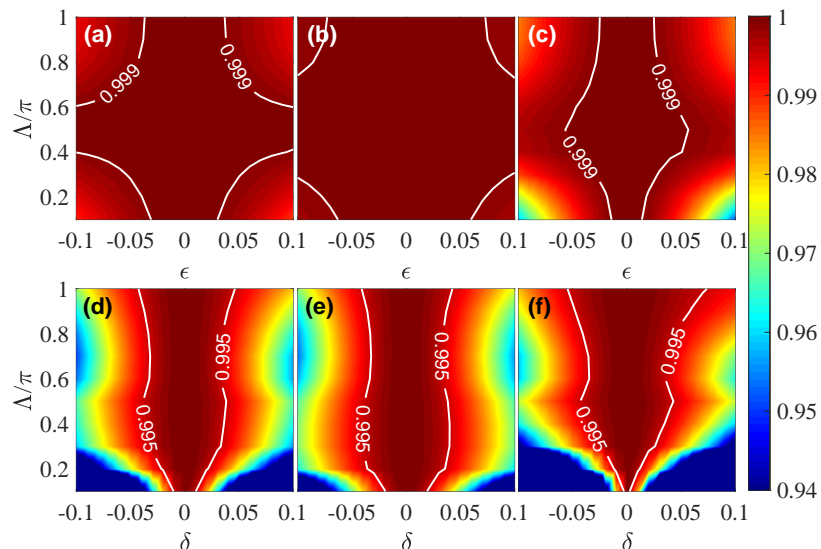


FIG. 3. Gate fidelities for geometric S, T and H gates as function of path parameters  $\Lambda$ , (a-c)  $\sigma_x$  and (d-f)  $\sigma_z$  errors with error fractions  $\epsilon, \delta \in [-0.1, 0.1]$ , without decoherence.

$\mathcal{A}_z = |1\rangle_1\langle 1| + 2|2\rangle_1\langle 2|$ , and  $\kappa_-$ ,  $\kappa_z$  are the relaxation and dephasing rate, respectively.

The gate fidelity is defined as  $F_1^G = \frac{1}{2\pi} \int_0^{2\pi} \langle \varphi_1^f | \rho_1 | \varphi_1^f \rangle d\theta_1$  [50] with the ideal final state of  $|\varphi_1^f\rangle = U_1|\varphi_1^i\rangle$ , the integration is numerically done for 1001 different initial states of  $|\varphi_1^i\rangle = \cos\theta_1|0\rangle + \sin\theta_1|1\rangle$  with  $\theta_1$  being uniformly distributed within the range of  $[0, 2\pi]$ . Besides, for stronger driving field, faster gate operation can be induced, and thus leads to less decoherence induced gate error. However, stronger driving field also causes more leakage to the non-computational subspace. Therefore, in figure 5, we plot the gate fidelities as a function of the pulse peak  $\Omega_0$  for geometric S, T and H gates with their optimal path parameters, i.e.,  $\Lambda = (0.42, 0.33, 0.5)\pi$ , where they have the highest fidelities in the configuration A. Meanwhile, for geometric H gate from configuration B, the optimal path parameter is  $\Lambda = 0.70\pi$ , which has the strongest robustness against  $\sigma_z$  error. Moreover, in the simulation, we have used a corrected shape  $\Omega_D(t) = \Omega(t) - \{i\dot{\Omega}(t) + [\dot{\phi}(t) + \Delta(t)]\Omega(t)\}/(2\alpha)$  for the driving field with the original simple pulse shape being  $\Omega(t) = \Omega_0 \sin^2(\pi t/T)$ , and decay rate of the transmon as  $\kappa_- = \kappa_z = 2\pi \times 4$  kHz,  $\alpha = 2\pi \times 220$  MHz [51]. By these setting, the maximal fidelities of S, T and H gates can be obtained as  $F_S^G \simeq 99.93\%$ ,  $F_T^G \simeq 99.95\%$  and  $F_H^G \simeq 99.95\%$  ( $\simeq 99.90\%$  for configuration B), and their corresponding uncorrected pulse peaks are  $\Omega_0/(2\pi) = (19, 24, 30)$  MHz, respectively. Finally, based on the optimal pulse peaks and path parameters above-mentioned, as shown in figure 6, we also plot the comparison of gate robustness between geometric gates and their corresponding dynamical ones against two local errors, in the form of  $(1 + \epsilon)\Omega(t)$  and  $\Delta + \delta\Omega_0$ .

### III. NONTRIVIAL TWO-QUBIT GEOMETRIC GATES OF PATH OPTIMIZATION

The above path-optimized method can be readily generalized to the case of nontrivial two-qubit geometric gates. As shown in figure 1(b), we here consider a two-dimensional lattice of adjacently capacitive coupled transmon qubits, and the coupling strength there is usually fixed once the chip is fabricated. To realize tunable coupling [53–56] between two qubits, e.g.,  $T_1$  and  $T_2$ , we add an ac driving of  $F(t) = \epsilon \sin(\nu t + \varphi(t))$  on the qubit  $T_2$  so that  $\omega_2(t) = \omega_2 + F(t)$ , and the interaction Hamiltonian can be calculated as

$$\mathcal{H}_{12}(t) = g_{12} \left\{ [|10\rangle_{12}\langle 01| e^{i\Delta_1 t} + \sqrt{2}|11\rangle_{12}\langle 02| e^{i(\Delta_1 + \alpha_2)t} + \sqrt{2}|20\rangle_{12}\langle 11| e^{i(\Delta_1 - \alpha_1)t}] e^{i\beta \cos[\nu t + \varphi(t)]} + \text{H.c.} \right\}, \quad (19)$$

where  $\Delta_1 = \omega_1 - \omega_2$  with  $\omega_1$  and  $\omega_2$  being the frequencies of qubits  $T_1$  and  $T_2$  respectively,  $\beta = \epsilon/\nu$ ,  $g_{12}$  is coupling constant, and  $\alpha_1$  and  $\alpha_2$  are the intrinsic anharmonicities of the two qubits. Making a representation transformation  $U = \exp\{-i\Delta'(|11\rangle_{12}\langle 11| - |02\rangle_{12}\langle 02|)t/2\}$  on  $\mathcal{H}_{12}(t)$ , and Hamiltonian  $\mathcal{H}_{12}(t)$  reduces to

$$\mathcal{H}'_{12}(t) = -\frac{1}{2} \left\{ \Delta' \cdot \sigma'_z - g'_{12} [\cos \varsigma(t) \sigma'_x + \sin \varsigma(t) \sigma'_y] \right\}, \quad (20)$$

where  $g'_{12} = 2\sqrt{2}g_{12}J_1(\beta)$ ,  $\Delta' = \nu - \Delta_1 - \alpha_2$ ,  $\varsigma(t) = \varphi(t) - \pi/2$ , and  $\{\sigma'_x, \sigma'_y, \sigma'_z\}$  are the Pauli operators represented by the subspace  $\{|11\rangle_{12}, |02\rangle_{12}\}$ . This represents a detuned interaction in the subspace of  $\{|11\rangle_{12}, |02\rangle_{12}\}$ , and whose structure of energy levels is plotted in figure 1(c). Note that we have utilized the Jacobi-Anger identity  $\exp[i\beta \cos(\nu t + \varphi(t))] =$

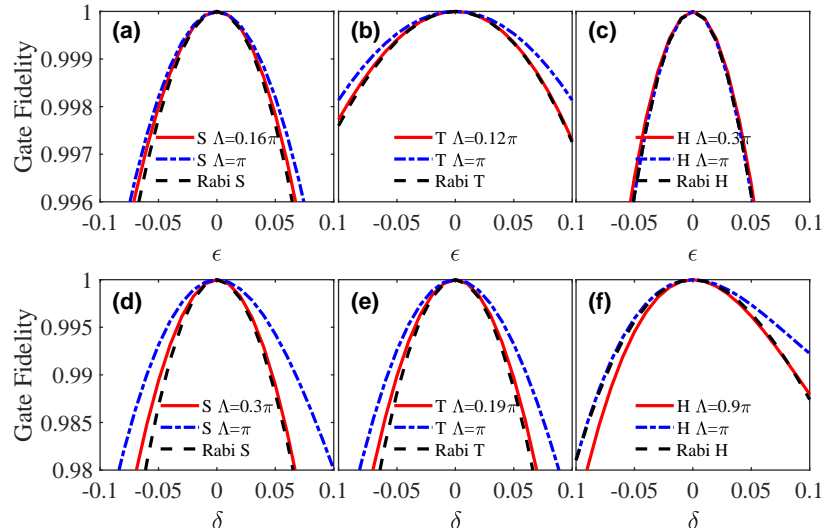


FIG. 4. The comparison of robustness between geometric S, T and H gates and their corresponding dynamical gates (denoted as “Rabi gates”) for two local errors, i.e., (a-c)  $\sigma_x$  and (d-f)  $\sigma_z$  errors, for their boundary paths, respectively.

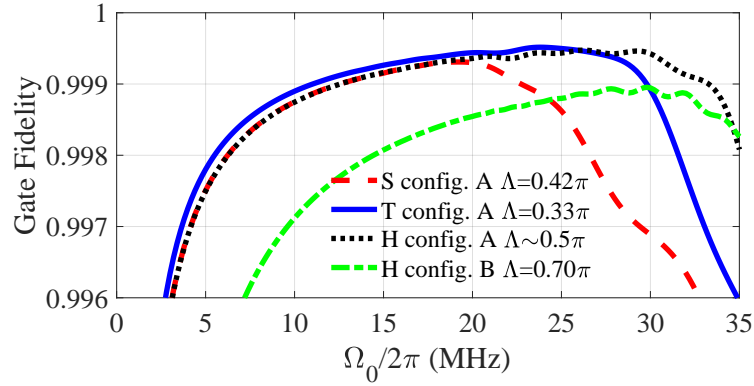


FIG. 5. The gate fidelities as a function of the pulse peak  $\Omega_0$  for geometric S, T and H gates with their optimal path parameters (S gate:  $\Lambda = 0.42\pi$ , T gate:  $\Lambda = 0.33\pi$ , H gate:  $\Lambda \simeq 0.5\pi$ ), which has the highest fidelities in the configuration A. For the configuration B, the optimal path parameter for the geometric H gate is  $\Lambda = 0.70\pi$ .

$\sum_{m=-\infty}^{\infty} i^m J_m(\beta) \exp[i m(\nu t + \varphi(t))]$  in obtaining equation (20). Obviously, Hamiltonian  $\mathcal{H}'_{12}(t)$  has the same structure as that of Hamiltonian  $\mathcal{H}_1(t)$  in the single-qubit case. Therefore, we can construct arbitrary single-qubit-like geometric gates in the subspace  $\{|11\rangle_{12}, |02\rangle_{12}\}$  through setting appropriate parameters, which corresponds to a two-qubit geometric control-phase gate in the two-qubit computational subspace  $\{|00\rangle_{12}, |01\rangle_{12}, |10\rangle_{12}, |11\rangle_{12}\}$ , i.e.,

$$U_2(\tau') = |00\rangle_{12}\langle 00| + |01\rangle_{12}\langle 01| + |10\rangle_{12}\langle 10| + e^{i\gamma_g''} |11\rangle_{12}\langle 11|. \quad (21)$$

In the following, we set  $\gamma_g'' = -\pi/4$  as a typical example to test this gate performance, whose path can be optimized similar to the single-qubit case. Then, the master equation can be rewritten as

$$\dot{\rho}_2 = -i[\mathcal{H}_{12}(t), \rho_2] + \frac{1}{2} \sum_{j=1}^2 \left\{ \kappa_z^j \mathcal{L}(\mathcal{A}_z^j) + \kappa_-^j \mathcal{L}(\mathcal{A}_-^j) \right\}, \quad (22)$$

where  $\mathcal{A}_-^j = |0\rangle_j\langle 1| + \sqrt{2}|1\rangle_j\langle 2|$  and  $\mathcal{A}_z^j = |1\rangle_j\langle 1| + 2|2\rangle_j\langle 2|$ . Besides, the two-qubit gate fidelity can be defined as  $F_2^G = \frac{1}{4\pi^2} \int_0^{2\pi} \int_0^{2\pi} \langle \varphi_2^f | \rho_2 | \varphi_2^f \rangle d\theta_1 d\theta_2$  for the ideal final state  $|\varphi_2^f\rangle = U_2|\varphi_2^i\rangle$  with a general initial state  $|\varphi_2^i\rangle = (\cos \theta_1 |0\rangle + \sin \theta_1 |1\rangle) \otimes$

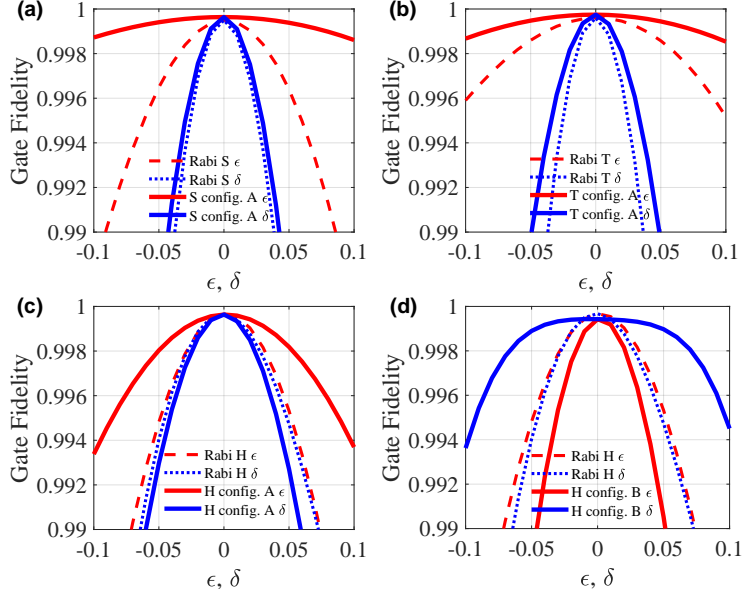


FIG. 6. Comparison of robustness between the geometric and corresponding dynamical gates against two local errors. (a-c) For the configuration A, gate-robustness for geometric S, T and H gates with the optimal path parameters (S gate:  $\Lambda = 0.42\pi$ , T gate:  $\Lambda = 0.33\pi$  and H gate:  $\Lambda \simeq 0.5\pi$ ) (d) The gate-robustness for geometric H gate with the optimal path parameter  $\Lambda = 0.70\pi$  in the configuration B.

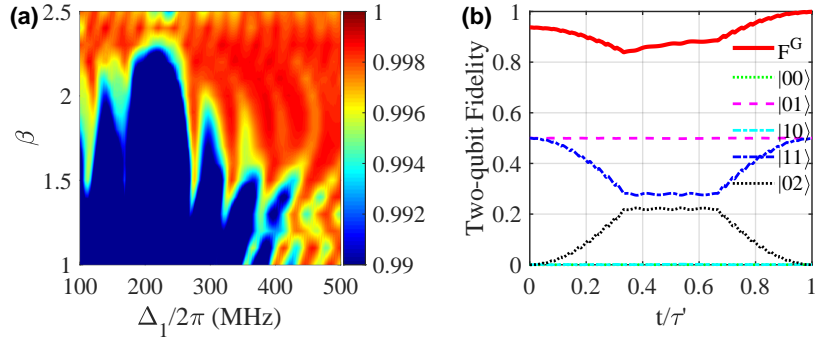


FIG. 7. (a) The gate fidelities of the implemented geometric control-phase gate ( $\gamma_g'' = -\pi/4$ ) as function of the parameters  $\Delta_1$  and  $\beta$  in the relative optimal path  $\Lambda = 0.45\pi$ . (b) The graph for corresponding state populations with the initial state  $(|01\rangle + |11\rangle)/\sqrt{2}$  and gate fidelity alter with the evolution time  $t$  in the same path as the (a).

$(\cos \theta_2 |0\rangle + \sin \theta_2 |1\rangle)$ , in which the integration is numerically performed for 10001 input states with  $\theta_1$  and  $\theta_2$  uniformly distributed in  $[0, 2\pi]$ . We set the relative optimal path  $\Lambda = 0.45\pi$  and plot the gate fidelity as a function of parameters  $\Delta_1$  and  $\beta$ , as shown in figure 7(a). We find that the two-qubit gate fidelities can exceed 99.85% when the parameters  $\beta$  and  $\Delta_1$  are around  $1.9 \pm 0.1$  and  $2\pi \times (388 \pm 5)$  MHz, respectively. Furthermore, in the figure 7(b), we plot the corresponding state populations and the gate fidelity dynamics with the initial state being  $(|01\rangle + |11\rangle)/\sqrt{2}$ , under the conditions of  $\beta = 1.9$  and  $\Delta_1 = 2\pi \times 388$  MHz, and the geometric control-phase gate fidelity can achieve as high as 99.87%. Moreover, in our numerical simulation, all parameters are set to be readily accessible within current transmon experiment [57], such as the coupling strength  $g_{12} = 2\pi \times 8$  MHz, transmon anharmonicities of  $\alpha_1 = \alpha_2 = 2\pi \times 220$  MHz,  $\kappa_z^1 = \kappa_z^2 = \kappa_-^1 = \kappa_-^2 = 2\pi \times 4$  kHz, and the detuning  $\Delta' \simeq -2\pi \times 83$  MHz. Note that, besides this high gate fidelity, the merit of gate robustness is similar as that of the case of single-qubit phase gate, as the structure of Hamiltonian  $\mathcal{H}'_{12}(t)$  is the same as that of  $\mathcal{H}_1(t)$ .

#### IV. CONCLUSION

In summary, we have proposed a path-optimized scheme for implementing nonadiabatic geometric gates on superconducting transmon qubits, where the constructed geometric S, T, and H gates are superior over the corresponding dynamical gates with regard to gate fidelity and robustness by selecting appropriate paths. Moreover, this method of path optimization can be readily generalized to the case of nontrivial two-qubit geometric gates, and the gate fidelity of geometric control-phase gate can reach 99.87% within the available experimental parameters. All of these merits suggest that our scheme represents a new perspective for large-scale fault-tolerant solid-state quantum computation.

#### ACKNOWLEDGEMENTS

This work was supported by the Key-Area Research and Development Program of GuangDong Province (Grant No. 2018B030326001), the National Natural Science Foundation of China (Grant No. 11874156), Guangdong Provincial Key Laboratory of Quantum Science and Engineering (Grant No. 2019B121203002), and Science and Technology Program of Guangzhou (Grant No. 2019050001).

#### APPENDIX A: THE CONSTRUCTION OF DYNAMICAL GATES

From a two-level quantum system that is resonant driving by an external field, the interaction Hamiltonian reads

$$\mathcal{H}_d(t) = \frac{1}{2}\Omega(t) [\cos \phi(t)\sigma_x + \sin \phi(t)\sigma_y], \quad (23)$$

we set  $\phi(t) = \phi_d$  as a constant, to ensure the geometric phase  $\gamma_g \equiv 0$ . Thus, the dynamical evolution operator at the final time  $\tau$  can be obtained as

$$U_d(\tau) = e^{-i \int_0^\tau \mathcal{H}_d(t) dt} = \sigma_z \cos \frac{\theta_{x,y}^d}{2} - i \sin \frac{\theta_{x,y}^d}{2} (\sigma_x \cos \phi_d + \sigma_y \sin \phi_d), \quad (24)$$

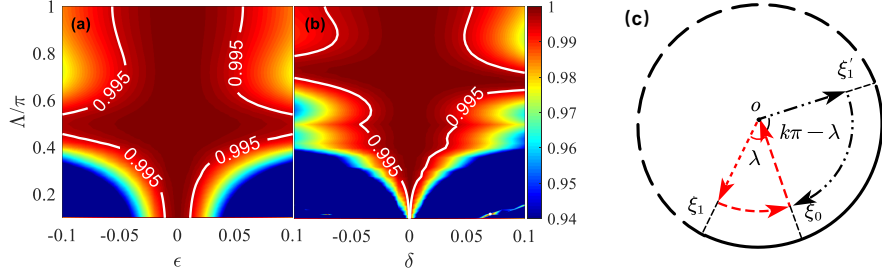


FIG. 8. Gate fidelities of the implemented geometric H gate for configuration B as a function of path parameters  $\Lambda$  for (a)  $\sigma_x$  and (b)  $\sigma_z$  errors without decoherence, respectively, with  $\epsilon, \delta \in [-0.1, 0.1]$ . (c) The vertical view of evolution trajectories in the Bloch sphere for configuration B (dash-dotted-black line) in contrast with the configuration A (dashed-red line).

where  $\theta_{x,y}^d = \int_0^\tau \Omega(t)dt$ . When  $\phi_d = 0$  and  $\pi/2$ , the  $X$ - and  $Y$ -axis rotation operations  $R_x^d(\theta_x^d)$  and  $R_y^d(\theta_y^d)$  can be obtained, respectively, while the  $Z$ -axis rotation can be obtained by  $R_z^d(\theta_z^d) = R_x^d(-\pi/2)R_y^d(-\theta_z^d)R_x^d(\pi/2)$ . Specially, a set of universal single-qubit gates, i.e., Phase,  $\pi/8$  and Hadamard gates can be realized as  $R_x^d(-\pi/2)R_y^d(-\pi/2)R_x^d(\pi/2)$ ,  $R_x^d(-\pi/2)R_y^d(-\pi/4)R_x^d(\pi/2)$  and  $R_x^d(\pi)R_y^d(\pi/2)$ , with total pulse areas  $\mathcal{S}_d = \int_0^\tau \Omega(t)dt = 3\pi/2, 5\pi/4$  and  $3\pi/2$ , respectively.

## APPENDIX B: GEOMETRIC QUANTUM GATES FROM CONFIGURATION B

Similar to those of the schemes in references [14, 36], there is also a path configuration B versus configuration A for our scheme. But the difference is that, in our scheme, the path configurations can be further optimized by choosing different path parameters  $\Lambda$ , while the former ones is only a special case of our scheme. Herein, in contrast to  $\xi_1 - \xi_0 = \lambda$  in the configuration A, we can set  $\xi'_1 - \xi_0 = \lambda - k\pi$  in the configuration B, which is shown in figure 8(c). Then, the geometric phase  $\gamma'_g$ , in the configuration B, can be calculated as

$$\gamma'_g = \frac{1}{2}(1 - \cos \Lambda)(\xi'_1 - \xi_0) = \gamma_g - \frac{k\pi(1 - \cos \Lambda)}{2}. \quad (25)$$

In this case, we let  $k\pi(1 - \cos \Lambda)/2 = \pi$  and have  $k = 2/(1 - \cos \Lambda)$ . Specially, when  $\Lambda = \pi$ , then  $\xi'_1 - \xi_0 = \lambda - \pi$ , which reduces to the configuration B for the conventional nonadiabatic GQC [14, 36]. As a result, the new evolution operator is  $U'_1(\tau) = \exp(i\gamma'_g \vec{n} \cdot \vec{\sigma}) = -\exp(i\gamma_g \vec{n} \cdot \vec{\sigma})$  that is equivalent to  $U_1(\tau)$  in the configuration A. Therefore, similar to the configuration A case, we can also optimize geometric quantum gates induced from configuration B, just changing  $\xi_1$  to  $\xi'_1$  in the path parameter.

For the  $\sigma_z$  error, in the configuration A case, as shown in the maintext, there is no range of the path parameter that makes the robustness of geometric H gate is better than that of the corresponding dynamical gate. Here, we only consider the robustness of path-optimized geometric H gate in the configuration B. As shown in figures 8(a) and 8(b), we can clearly obtain the gate robustness for geometric H gate is distinct within the range of  $\Lambda/\pi \in [0.1, 0.5) \cup (0.5, 1]$  under two different local errors  $\epsilon, \delta \in [-0.1, 0.1]$ . Moreover, in figures 9(a) and 9(b), we compare the robustness of this gate with its corresponding dynamical gate under several boundary paths. We find that the geometric quantum gates possess better robustness when the path parameter

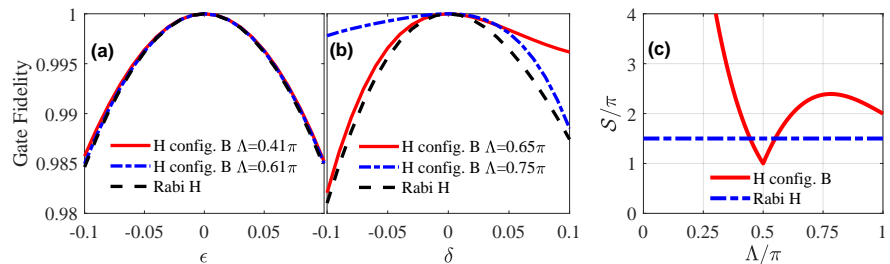


FIG. 9. Comparison of robustness between geometric H gate and corresponding dynamical gate (also denoted as “Rabi gate”) against (a)  $\sigma_x$  and (b)  $\sigma_z$  errors for the boundary path parameters, respectively. (c) The comparison of the total pulse areas  $\mathcal{S}$  for geometric H gate in the configuration B case with different path parameters and the corresponding dynamical gate.

is within the ranges of  $\Lambda/\pi \in [0.41, 0.5) \cup (0.5, 0.61]$  and  $\Lambda/\pi \in [0.65, 0.75]$  for  $\sigma_x$  and  $\sigma_z$  errors, respectively. Obviously, it can be found that the stronger robustness against  $\sigma_z$  error is, the weaker robustness against  $\sigma_x$  error will be, which is just opposite to the result in the configuration A case. In addition, in the case of the configuration B, the pulse areas for geometric and dynamical H gate as a function of the path parameter  $\Lambda/\pi \in (0, 0.5) \cup (0.5, 1]$  are plotted in figure 9(c).

## REFERENCES

- [1] Lloyd S 1995 Almost Any Quantum Logic Gate is Universal *Phys. Rev. Lett.* **75** 346
- [2] Barenco A, Bennett C H, Cleve R, DiVincenzo D P, Margolus N, Shor P, Sleator T, Smolin J A, and Weinfurter H 1995 Elementary gates for quantum computation *Phys. Rev. A* **52** 3457
- [3] Berry M V 1984 Quantal phase factors accompanying adiabatic change *Proc. R. Soc. Lond. A* **392** 45
- [4] Ekert A, Ericsson M, Hayden P, Inamori H, Jones J A, Oi D K L, and Vedral V 2000 Geometric quantum computation *J. Mod. Opt.* **47** 2501
- [5] Jones J A, Vedral V, Ekert A and Castagnoli G 2000 Geometric quantum computation using nuclear magnetic resonance *Nature* **403** 869
- [6] Wu H, Gauger E M, George R E, Möttönen M, Riemann H, Abrosimov N V, Becker P, Pohl H-J, Itoh K M, Thewalt M L W, and Morton J J L 2013 Geometric phase gates with adiabatic control in electron spin resonance *Phys. Rev. A* **87** 032326
- [7] Huang Y-Y, Wu Y-K, Wang F, Hou P-Y, Wang W-B, Zhang W-G, Lian W-Q, Liu Y-Q, Wang H-Y, Zhang H-Y, He L, Chang X-Y, Xu Y, and Duan L-M 2019 Experimental Realization of Robust Geometric Quantum Gates with Solid-State Spins *Phys. Rev. Lett.* **122** 010503
- [8] Aharonov Y and Anandan J 1987 Phase change during a cyclic quantum evolution *Phys. Rev. Lett.* **58** 1593
- [9] Wang X B and Keiji M 2001 Nonadiabatic Conditional Geometric Phase Shift with NMR *Phys. Rev. Lett.* **87** 097901
- [10] Zhu S L and Wang Z D 2002 Implementation of Universal Quantum Gates Based on Nonadiabatic Geometric Phases *Phys. Rev. Lett.* **89** 097902
- [11] Zhu S L and Wang Z D 2003 Unconventional geometric quantum computation *Phys. Rev. Lett.* **91** 187902
- [12] Leibfried D, DeMarco B, Meyer V, Lucas D, Barrett M, Britton J, Itano W M, Jelenković B, Langer C, Rosenband T, and Wineland D J 2003 Experimental demonstration of a robust, high-fidelity geometric two ion-qubit phase gate *Nature (London)* **422** 412
- [13] Du J F, Zou P and Wang Z D 2006 Experimental implementation of high-fidelity unconventional geometric quantum gates using an NMR interferometer *Phys. Rev. A* **74** 020302(R)
- [14] Xu Y, Hua Z, Chen T, Pan X, Li X, Han J, Cai W, Ma Y, Wang H, Song Y, Xue Z-Y, and Sun L 2020 Experimental Implementation of Universal Nonadiabatic Geometric Quantum Gates in a Superconducting Circuit *Phys. Rev. Lett.* **124** 230503
- [15] Wilczek F and Zee A 1984 Appearance of gauge structure in simple dynamical systems *Phys. Rev. Lett.* **52** 2111
- [16] Zanardi P and Rasetti M 1999 Holonomic Quantum Computation *Phys. Lett. A* **264** 94
- [17] Pachos J, Zanardi P, and Rasetti M 1999 Non-Abelian Berry connections for quantum computation *Phys. Rev. A* **61** 010305(R)
- [18] Duan L M, Cirac J I and Zoller P 2001 Geometric Manipulation of Trapped Ions for Quantum Computation *Science* **292** 1695
- [19] Sjöqvist E, Tong D M, Andersson L M, Hessmo B, Johansson M, and Singh K 2012 Non-adiabatic holonomic quantum computation *New J. Phys.* **14** 103035
- [20] Xu G F, Zhang J, Tong D M, Sjöqvist E and Kwek L C 2012 Nonadiabatic Holonomic Quantum Computation in Decoherence-Free Subspaces *Phys. Rev. Lett.* **109** 170501
- [21] Chiara G D and Palma G M 2003 Berry Phase for a Spin 1/2 Particle in a Classical Fluctuating Field *Phys. Rev. Lett.* **91** 090404
- [22] Solinas P, Zanardi P and Zanghì N 2004 Robustness of non-Abelian holonomic quantum gates against parametric noise *Phys. Rev. A* **70** 042316
- [23] Zhu S-L and Zanardi P 2005 Geometric quantum gates that are robust against stochastic control errors *Phys. Rev. A* **72** 020301(R)
- [24] Filipp S, Klepp J, Hasegawa Y, Plonka-Spehr C, Schmidt U, Geltenbort P, and Rauch H 2009 Experimental Demonstration of the Stability of Berry's Phase for a Spin-1/2 Particle *Phys. Rev. Lett.* **102** 030404
- [25] Johansson M, Sjöqvist E, Andersson L M, Ericsson M, Hessmo B, Singh K, and Tong D M 2012 Robustness of nonadiabatic holonomic gates *Phys. Rev. A* **86** 062322
- [26] Solinas P, Zanardi P, Zanghì N and Rossi F 2003 Nonadiabatic geometrical quantum gates in semiconductor quantum dots *Phys. Rev. A* **67** 052309
- [27] Ota Y and Kondo Y 2009 Composite pulses in NMR as nonadiabatic geometric quantum gates *Phys. Rev. A* **80** 024302
- [28] Thomas J T, Lababidi M and Tian M 2011 Robustness of single-qubit geometric gate against systematic error *Phys. Rev. A* **84** 042335
- [29] Zhang X D, Zhu S L, Hu L and Wang Z D 2005 Nonadiabatic geometric quantum computation using a single-loop scenario *Phys. Rev. A* **71** 014302
- [30] Xu G F and Long G L 2014 Universal Nonadiabatic Geometric Gates in Two-Qubit Decoherence-Free Subspaces *Sci. Rep.* **4** 6814
- [31] Zhao P Z, Cui X D, Xu G F, Sjöqvist E and Tong D M 2017 Rydberg-atom-based scheme of nonadiabatic geometric quantum computation *Phys. Rev. A* **96** 052316
- [32] Chen T and Xue Z Y 2018 Nonadiabatic Geometric Quantum Computation with Parametrically Tunable Coupling *Phys. Rev. Appl.* **10** 054051
- [33] Zhang C, Chen T, Li S, Wang X and Xue Z Y 2020 High-fidelity geometric gate for silicon-based spin qubits *Phys. Rev. A* **101** 052302

- [34] Li K Z, Zhao P Z, and Tong D M 2020 Approach to realizing nonadiabatic geometric gates with prescribed evolution paths *Phys. Rev. Res.* **2** 023295
- [35] Li S, Xue J, Chen T, and Xue Z-Y 2021 High-fidelity geometric quantum gates with short paths on superconducting circuits *Adv. Quantum Technol.* **4** 2000140
- [36] Zhou J, Li S, Pan G-Z, Zhang G, Chen T, and Xue Z-Y 2021 Nonadiabatic geometric quantum gates that are insensitive to qubit-frequency drifts *Phys. Rev. A* **103** 032609
- [37] Zhang C, Chen T, Wang X, and Xue Z-Y 2021 Implementation of geometric quantum gates on microwave-driven semiconductor charge qubits *Adv. Quantum Technol.* **4** 2100011
- [38] Friedenauer A and Sjöqvist E 2003 Noncyclic geometric quantum computation *Phys. Rev. A* **67** 024303
- [39] Wang Z S, Liu G Q and Ji Y H 2009 Noncyclic geometric quantum computation in a nuclear-magnetic-resonance system *Phys. Rev. A* **79** 054301
- [40] Liu B J, Su S L and Yung M H 2020 Nonadiabatic noncyclic geometric quantum computation in Rydberg atoms *Phys. Rev. Res.* **2** 043130
- [41] Lv Q-X, Liang Z-T, Liu H-Z, Liang J-H, Liao K-Y, and Du Y-X 2020 Noncyclic geometric quantum computation with shortcut to adiabaticity *Phys. Rev. A* **101** 022330
- [42] Chen T and Xue Z Y 2020 High-Fidelity and Robust Geometric Quantum Gates that Outperform Dynamical Ones *Phys. Rev. Appl.* **14** 064009
- [43] Ji L-N, Ding C-Y, Chen T, and Xue Z-Y 2021 Noncyclic Geometric Quantum Gates with Smooth Paths via Invariant-Based Shortcuts *Adv. Quantum Technol.* **4** 2100019
- [44] Koch J, Yu T M, Gambetta J, Houck A A, Schuster D I, Majer J, Blais A, Devoret M H, Girvin S M, and Schoelkopf R J 2007 Charge-insensitive qubit design derived from the Cooper pair box *Phys. Rev. A* **76** 042319
- [45] You J Q, Hu X, Ashhab S and Nori F 2007 Low-decoherence flux qubit *Phys. Rev. B* **75** 140515(R)
- [46] Wang X G, Sun Z and Wang Z D 2009 Operator fidelity susceptibility: An indicator of quantum criticality *Phys. Rev. A* **79** 012105
- [47] Motzoi F, Gambetta J M, Rebentrost P and Wilhelm F K 2009 Simple Pulses for Elimination of Leakage in Weakly Nonlinear Qubits *Phys. Rev. Lett.* **103** 110501
- [48] Gambetta J M, Motzoi F, Merkel S T and Wilhelm F K 2011 Analytic control methods for high-fidelity unitary operations in a weakly nonlinear oscillator *Phys. Rev. A* **83** 012308
- [49] Lindblad G 1976 On the generators of quantum dynamical semigroups *Commun. Math. Phys.* **48** 119
- [50] Poyatos J F, Cirac J I and Zoller P 1997 Complete Characterization of a Quantum Process: The Two-bit Quantum Gate *Phys. Rev. Lett.* **78** 390
- [51] Barends R, Kelly J, Megrant A, Veitia A, Sank D, Jeffrey E, White T C, Mutus J, Fowler A G, Campbell B, Chen Y, Chen Z, Chiaro B, Dunsworth A, Neill C, O’Malley P, Roushan P, Vainsencher A, Wenner J, Korotkov A N, Cleland A N, and Martinis J M 2014 Superconducting quantum circuits at the surface code threshold for fault tolerance *Nature* **508** 500
- [52] Chen Z, Kelly J, Quintana C, Barends R, Campbell B, Chen Y, Chiaro B, Dunsworth A, Fowler A G, Lucero E, Jeffrey E, Megrant A, Mutus J, Neeley M, Neill C, O’Malley P J J, Roushan P, Sank D, Vainsencher A, Wenner J, White T C, Korotkov A N, and Martinis J M 2016 Measuring and Suppressing Quantum State Leakage in a Superconducting Qubit *Phys. Rev. Lett.* **116** 020501
- [53] Roth M, Ganzhorn M, Moll N, Filipp S, Salis G, and Schmidt S 2017 Analysis of a parametrically driven exchange-type gate and a two-photon excitation gate between superconducting qubits *Phys. Rev. A* **96** 062323
- [54] Li X, Ma Y, Han J, Chen T, Xu Y, Cai W, Wang H, Song Y P, Xue Z-Y, Yin Z-q, Sun L 2018 Perfect Quantum State Transfer in a Superconducting Qubit Chain with Parametrically Tunable Couplings *Phys. Rev. Appl.* **10** 054009
- [55] Cai W, Han J, Mei F, Xu Y, Ma Y, Li X, Wang H, Song Y P, Xue Z-Y, Yin Z-q, Jia S, and Sun L 2019 Observation of Topological Magnon Insulator States in a Superconducting Circuit *Phys. Rev. Lett.* **123** 080501
- [56] Chu J, Li D, Yang X, Song S, Han Z, Yang Z, Dong Y, Zheng W, Wang Z, Yu X, Lan D, Tan X, and Yu Y 2020 Realization of Superadiabatic Two-Qubit Gates Using Parametric Modulation in Superconducting Circuits *Phys. Rev. Appl.* **13** 064012
- [57] Kjaergaard M, Schwartz M E, Braumüller J, Krantz P, Wang J I-J, Gustavsson S, and Oliver W D 2020 Superconducting Qubits: Current State of Play *Annu. Rev. Condens. Matter Phys.* **11** 369